PAPER

Check for updates

Phase separation dynamics in deformable droplets†

Simon Gsell [ID] [ab] and Matthias Merkel [ID] *[a]

Phase separation can drive spatial organization of multicomponent mixtures. For instance in developing animal embryos, effective phase separation descriptions have been used to account for the spatial organization of different tissue types. Similarly, separation of different tissue types is also observed in stem cell aggregates, where the emergence of a polar organization can mimic early embryonic axis formation. Here, we describe such aggregates as deformable two-phase fluid droplets, which are suspended in a fluid environment (third phase). Using hybrid finite-volume Lattice-Boltzmann simulations, we numerically explore the out-of-equilibrium routes that can lead to the polar equilibrium state of such a droplet. We focus on the interplay between spinodal decomposition and advection with hydrodynamic flows driven by interface tensions, which we characterize by a Peclet number Pe. Consistent with previous work, for large Pe the coarsening process is generally accelerated. However, for intermediate Pe we observe long-lived, strongly elongated droplets, where both phases form an alternating stripe pattern. We show that these "croissant" states are close to mechanical equilibrium and coarsen only slowly through diffusive fluxes in an Ostwald-ripening-like process. Finally, we show that a surface tension asymmetry between both droplet phases leads to transient, rotationally symmetric states whose resolution leads to flows reminiscent of Marangoni flows. Our work highlights the importance of advection for the phase separation process in finite, deformable systems.

1 Introduction

Systems composed of two or more components can undergo phase separation.[1–3] During this process, phase domains of different composition first emerge either through spinodal decomposition or nucleation, before these domains coarsen through diffusive processes such as Ostwald ripening. Coarsening is associated with a power-law growth of typical domain size λ, which scales as $\lambda \sim t^{1/3}$ with time t.[1] In the case of fluid–fluid phase separation, coarsening can also occur through advection with hydrodynamic flows that are driven by the interface tension between adjacent domains. Such hydrodynamic flows can speed up domain coarsening, which can lead to *e.g.* a linear scaling $\lambda \sim t$.[1] However, the precise interplay between diffusive and hydrodynamic processes can be quite complex, leading to a rich phenomenology.[4]

While phase separation has long been employed for industrial processes, it has also been identified as a key organizing mechanism in biological systems, from the sub-cellular[5] to the ecological[6] scale. For example, the interior of biological cells is organized in part through fluid compartments that can emerge from phase separation.[5,7,8] Phase separation has moreover been used as effective model to describe the formation of multi-cellular aggregates.[9] But it has also been used to describe separation of different types of biological tissues.[10–13] This was motivated by experiments showing that different embryonic cell populations can unmix.[14,15] Moreover, given that embryonic tissues and aggregates often behave like viscous liquids on long times,[15–21] unmixing of cell populations could also be accelerated by long-range hydrodynamic flows.

Phase separation of biological tissues could also help to understand an important question in the field of developmental biology: How does the vertebrate axis form during animal development? To address this and related questions, experimentalists study aggregates of stem cells, called gastruloids, which have been shown to mimic vertebrate development (Fig. 1a and b).[22–24] Such gastruloids initially consist of spherical aggregates of undifferentiated stem cells (Fig. 1a). Even under isotropic boundary conditions, these aggregates then reliably[25] form polarized structures with different cell populations (Fig. 1b).[26] This process has been related to the definition of the axis of the vertebral column *in vivo*.[23,27] However, how exactly this axis initially emerges has remained unclear.

[a] *Aix Marseille Univ, Université de Toulon, CNRS, CPT (UMR 7332), Turing Centre for Living Systems, Marseille, France. E-mail: simon.gsell@univ-amu.fr, matthias.merkel@cnrs.fr*

[b] *Aix Marseille Univ, CNRS, IBDM (UMR 7288), Turing Centre for Living Systems, Marseille, France*

† Electronic supplementary information (ESI) available. See DOI: 10.1039/d1sm01647d
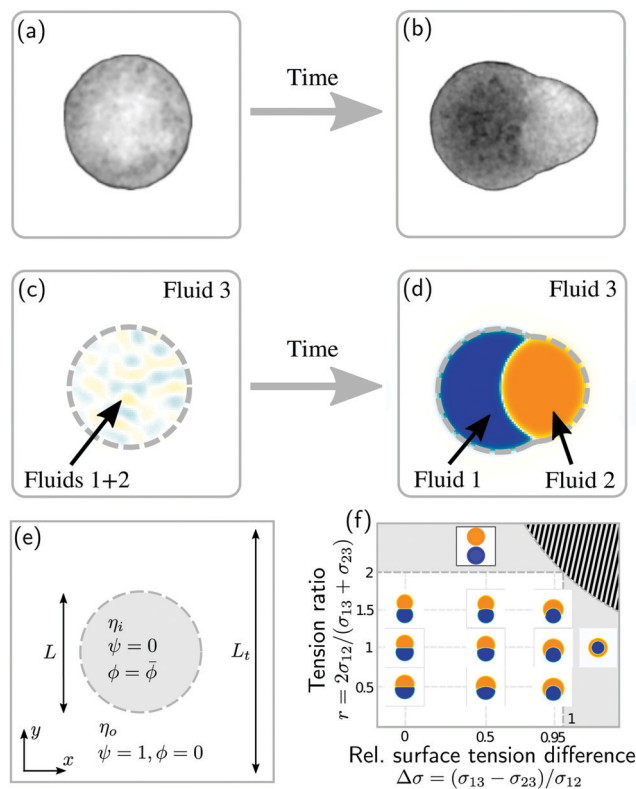
Fig. 1 Phase separation and symmetry breaking in deformable multi-component droplets. (a and b) Microscopy images of cell aggregates mimicking early vertebrate development, taken 1 day apart from each other. Brighter regions indicate the early mesoderm marker T/Brachyury (images taken from ref. 26). (c–e) Ternary fluid mixture model: a droplet, immersed in fluid 3 and initially composed of a mixture of fluids 1 and 2 (c), undergoes phase-separation until reaching the thermodynamic equilibrium state (d) characterized by a surface tension balance between all interfaces. (e) Schematic representation of the physical configuration. (f) Dependence of the thermodynamic equilibrium state on the inner-to-outer tension ratio $r = 2\sigma_{12}/(\sigma_{13} + \sigma_{23})$ and the relative surface tension difference $\Delta\sigma = (\sigma_{13} - \sigma_{23})/\sigma_{12}$. The hatched region marks an unphysical regime, because at least one of the tensions σ_{ij} would need to be negative there.

As a first step towards building a better physical understanding of such cellular aggregates, we study here the passive dynamics of a ternary phase-separating system (Fig. 1c–e), where a droplet made out of two fluid phases (1 and 2) is suspended in a third fluid phase (3). There is a limited number of possibilities for the thermodynamic equilibrium state of such a ternary system, depending on the ratios of the interface tension σ_{12} to the surface tensions σ_{13} and σ_{23} (Fig. 1f). Here, we focus on the case where the equilibrium state is a Janus droplet (Fig. 1d), i.e. where $\sigma_{12} < \sigma_{13} + \sigma_{23}$ and $|\sigma_{13} - \sigma_{23}| < \sigma_{12}$ (white region in Fig. 1f). While the equilibrium state is well known, we are interested in the dynamics that leads to this state, and how it depends on the interplay between diffusion and hydrodynamic flows. We start from an initial state where fluids 1 and 2 are almost homogeneously mixed inside of a spherical droplet (Fig. 1c). Thus, during the phase separation process, the system needs to spontaneously break rotational symmetry to reach the polarized equilibrium state (Fig. 1d).

Here, we numerically study the dynamics of this ternary system using 2D hybrid finite-volume Lattice-Boltzmann simulations of coupled Cahn-Hilliard and Stokes equations. We study the system's dynamics in terms of a Peclet number Pe that characterizes the magnitude of hydrodynamic advection as compared to diffusive effects. We find that while increasing Pe generally speeds up the phase separation process, intermediate Pe give rise to long-lived "croissant" states that slow down the relaxation to the final polarized state. When including an asymmetry between the surface tensions σ_{13} and σ_{23}, transient polar Marangoni flows are created, but the overall Pe-dependency remains. Taken together, our work demonstrates the importance of hydrodynamic flows in deformable multi-phase droplets.

Note that our study does not constitute a complete description of the polarization of stem cell aggregates. Rather, we study the interaction of two effects that likely are important for this process: unmixing of cell populations and interface-tension-driven advection. This lays ground work for constructing effective physical descriptions for the collective cellular behavior in stem cell aggregates (see Section 5).

2 Model

2.1 Free energy

We describe a 2D ternary system where the three components have area fractions C_1, C_2, and C_3, which sum up to one everywhere:

$$C_1 + C_2 + C_3 = 1. \tag{1}$$

To describe the phase-separating behavior of these three components, we use the following generic free energy:[28]

$$\mathcal{F} = \int_\Omega \left[\frac{\kappa_1}{2} C_1^2 (1 - C_1)^2 + \frac{\kappa_2}{2} C_2^2 (1 - C_2)^2 + \frac{\kappa_3}{2} C_3^2 (1 - C_3)^2 \right.$$
$$\left. + \frac{\kappa_1'}{2} (\nabla C_1)^2 + \frac{\kappa_2'}{2} (\nabla C_2)^2 + \frac{\kappa_3'}{2} (\nabla C_3)^2 \right] \mathrm{d}A. \tag{2}$$

The integral is over the total system area Ω. For each component $j \in \{1,2,3\}$, the free energy thus includes a quartic double-well potential with local minima at $C_j = 0$ and $C_j = 1$, and an energy density scale κ_j. Moreover, gradient terms with coefficients κ_j' ensure finite widths of all interfaces. For any binary interface between phases of dominating components j and k, i.e. where the third area fraction vanishes, interface width α_{jk} and interface tension σ_{jk} take on the well-known values:[28]

$$\alpha_{jk} = \sqrt{\frac{\kappa_j' + \kappa_k'}{\kappa_j + \kappa_k}} \quad \text{and} \quad \sigma_{jk} = \frac{\alpha_{jk}}{6}(\kappa_j + \kappa_k). \tag{3}$$

In the following, we will use the same width $\alpha = \alpha_{jk}$ for all interfaces $jk \in \{12,13,23\}$.

2.2 Dynamic equations

To define the dynamics of the area fractions C_j such that eqn (1) remains fulfilled, we follow Semprebon et al.[28] by introducing phase fields ϕ and ψ as

$$\phi = C_1 - C_2 \quad \text{and} \quad \psi = C_3. \tag{4}$$

Using these definitions together with eqn (1), the free energy in eqn (2) can be expressed in terms of ϕ and ψ instead of the C_j:[28]

$$\mathcal{F} = \int_\Omega \left[\frac{\kappa_1}{32}(1 - \psi + \phi)^2 (1 + \psi - \phi)^2 \right.$$
$$+ \frac{\kappa_2}{32}(1 - \psi - \phi)^2 (1 + \psi + \phi)^2 + \frac{\kappa_3}{2}\psi^2(1 - \psi)^2$$
$$\left. + \frac{\kappa_1'}{8}(\nabla\phi - \nabla\psi)^2 + \frac{\kappa_2'}{8}(\nabla\phi + \nabla\psi)^2 + \frac{\kappa_3'}{2}(\nabla\psi)^2 \right] \mathrm{d}A. \tag{5}$$

We then choose Cahn-Hilliard dynamics for both ϕ and ψ:

$$\frac{\partial\phi}{\partial t} + \nabla\cdot(\boldsymbol{u}\phi) = \nabla\cdot([1 - \psi]\Gamma_\phi\nabla\mu_\phi) \tag{6a}$$

$$\frac{\partial\psi}{\partial t} + \nabla\cdot(\boldsymbol{u}\psi) = \nabla\cdot(\Gamma_\psi\nabla\mu_\psi), \tag{6b}$$

where t is time, $\boldsymbol{u}$ is the local fluid velocity, Γ_ϕ and Γ_ψ are mobility parameters, and $\mu_\phi = \delta\mathcal{F}/\delta\phi$ and $\mu_\psi = \delta\mathcal{F}/\delta\psi$ are the chemical potentials of ϕ and ψ, respectively. The factor $[1 - \psi]$ in eqn (6a) ensures that fluids 1 and 2 do not diffuse across fluid 3. This is motivated by the biological background – we exclude any dissociation and re-association of cells (components 1 and 2) from/to the aggregate.

To account for hydrodynamic effects, we describe all phases of the system as incompressible Newtonian fluids, using the incompressible Stokes' equations:

$$0 = \nabla\cdot\boldsymbol{u} \tag{7a}$$

$$0 = -\nabla\Pi + \nabla\cdot(2\eta\boldsymbol{S}) - \phi\nabla\mu_\phi - \psi\nabla\mu_\psi. \tag{7b}$$

Here, Π is the fluid pressure, η is the fluid viscosity, $\boldsymbol{S}$ is the shear-rate tensor $\boldsymbol{S} = (\nabla\boldsymbol{u} + (\nabla\boldsymbol{u})^T)/2$, and the last two terms correspond to the forces introduced by the scalar fields.[1] We focus here on overdamped dynamics, as this is the relevant limit for $\sim 100\ \mu$m scale cellular aggregates with shear rates on the $\sim$day^{-1} scale. Because the effective viscosity of embryonic cell aggregates is typically many orders of magnitude above that of water,[29] we choose a ψ-dependent viscosity $\eta(\psi) = (1 - \psi)\eta_i + \psi\eta_o$, where $\eta_i \gg \eta_o$.

2.3 Initial and boundary conditions

We initialize the 2D system in a configuration schematized in Fig. 1c and e. The system initially consists of a circular droplet with diameter L, composed of a mixture of fluids 1 and 2 with $\psi = 0$, which is surrounded by fluid 3 with $\psi = 1$ and $\phi = 0$. The inside of the droplet is initialized as $\phi = \bar\phi + \Delta\phi_{IC}\xi$, where $\bar\phi$ and $\Delta\phi_{IC}$ are scalar parameters, and ξ is zero-mean, delta-correlated Gaussian white noise. The parameter $\bar\phi$ corresponds to the conserved area average of ϕ, defined as

Table 1 Values of dimensionless parameters used in our simulations

Parameter	$\bar\phi$	L/α	r	Pe_ψ	η_i/η_o	$\Delta\phi_{IC}$	L_t/L	$\Delta x/\alpha$	$\Delta t/(\Delta x\eta_i/\sigma_{12})$
Value	0	64	1	15/32	20	0.01	2	1	1/640

$\bar\phi = \int_\Omega (1 - \psi)\phi\mathrm{d}A / \int_\Omega (1 - \psi)\mathrm{d}A$. We simulate the system in a squared periodic box with side length L_t. Parameter values are listed in Table 1.

2.4 Dimensionless parameters

2.4.1 Equilibrium state. The equilibrium state depends on four dimensionless parameters. These are first, the difference $\bar\phi$ in area fractions between fluids 1 and 2. Here we focus exclusively on the case $\bar\phi = 0$, i.e. each fluid occupies half of the droplet area. Second, we set the ratio between droplet size L and interface width α to $L/\alpha = 64$.

Finally, the equilibrium state also depends on the three tensions σ_{jk}, for which we choose the following two dimensionless ratios:

$$r = \frac{2\sigma_{12}}{\sigma_{13} + \sigma_{23}}, \quad \Delta\sigma = \frac{\sigma_{13} - \sigma_{23}}{\sigma_{12}}. \tag{8}$$

The parameter r is the ratio between the (inner) interface tension and the average of the (outer) surface tensions. Unless stated otherwise, we set $r = 1$. The parameter $\Delta\sigma$ quantifies the surface tension difference between fluids 1 and 2 with respect to fluid 3. In the following, $\Delta\sigma$ is varied over the range $0 < \Delta\sigma < 1$. We are thus in the regime where the equilibrium state is a dipole structure (Fig. 1f).

2.4.2 Relaxation dynamics. The four phenomenological coefficients Γ_ϕ, Γ_ψ, η_i, and η_o affect only the relaxation dynamics. Absorbing one to rescale time, we obtain three dimensionless parameters.

First, we define a Peclet number that compares advective fluxes due to hydrodynamic flows to the diffusive fluxes of the ϕ-field:

$$\mathrm{Pe} = \frac{L\alpha}{\Gamma_\phi\eta_i}. \tag{9}$$

This number is defined on the scale of the droplet size L; it corresponds to the ratio $\mathrm{Pe} = \tau_D/\tau_A$ between a diffusive time scale $\tau_D = L^2/D_\phi$ with the typical diffusion coefficient scale $D_\phi = \Gamma_\phi\sigma_{12}/\alpha \sim \Gamma_\phi(\kappa_1 + \kappa_2)$, and an advective time scale $\tau_A = L/v_f$ with the typical flow velocity scale $v_f = \sigma_{12}/\eta_i$. Increasing the Peclet number corresponds to increasing the influence of advection. The limit case $\mathrm{Pe} = 0$ is simulated by ignoring the advection term in eqn (6a) and (6b). In this case, we set $\Gamma_\phi/\Gamma_\psi = 3$. In this article, we will vary Pe to probe how the interplay of diffusion and hydrodynamic flows affects the phase separation dynamics.

Second, we define a Peclet number with respect to the ψ field, and with respect to the interface width α, as $\mathrm{Pe}_\psi = \alpha^2/(\Gamma_\psi\eta_i)$. Here, we fix this number to a relatively small value of $\mathrm{Pe}_\psi = 15/32$ to ensure that the outer droplet interface remains stable during the simulations.

Third, we fix the viscosity ratio between droplet and the surrounding fluid to the value $\eta_i/\eta_o = 20$. We have checked that changes of this ratio do not strongly affect the simulation results as long as $\eta_i/\eta_o \gtrsim 10$.

2.5 Numerical implementation

We solve the dynamical equations (6a)–(7b) using a hybrid finite-volume Lattice Boltzmann approach. Similar methods have been used in earlier publications,[30–32] which employed finite-difference schemes for the phase field dynamics. Here, we use a finite-volume scheme instead to ensure exact conservation of the scalar fields ϕ and ψ.[33]

We discretize space using a Cartesian square grid with spacing $\Delta x = \alpha$. For the advection terms in eqn (6a) and (6b), we use a first-order upwind scheme, and for the diffusive fluxes we use a central second-order scheme. We integrate over time using a first-order explicit Euler scheme. We solve the incompressible Stokes eqn (7a) and (7b) using a two-relaxation-time Lattice Boltzmann method.[34] While the Lattice Boltzmann method actually solves the Navier–Stokes equations, which include inertia, we treat the Reynolds number (*i.e.* inertia) as a small numerical parameter here. The time step for both finite-volume and Lattice Boltzmann parts is $\Delta t = (\Delta x/v_f)/640$ with the flow velocity scale $v_f = \sigma_{12}/\eta_i$. Details on the numerical method are provided in the ESI.†

3 Results

In the following, we examine how the droplet polarization dynamics depends (i) on the magnitude of advection as quantified by the Peclet number Pe (Sections 3.1 and 3.2) and (ii) on surface tension asymmetry, $\Delta\sigma \neq 0$ (Section 3.3).

3.1 Advection speeds up the polarization process

To study the role of advection for the phase separation process, we run simulations with symmetric surface tensions, $\Delta\sigma = 0$, and varying Peclet number Pe (Fig. 2, Movies S1–S3, ESI†). In all cases, the system reaches indeed the polar equilibrium state.
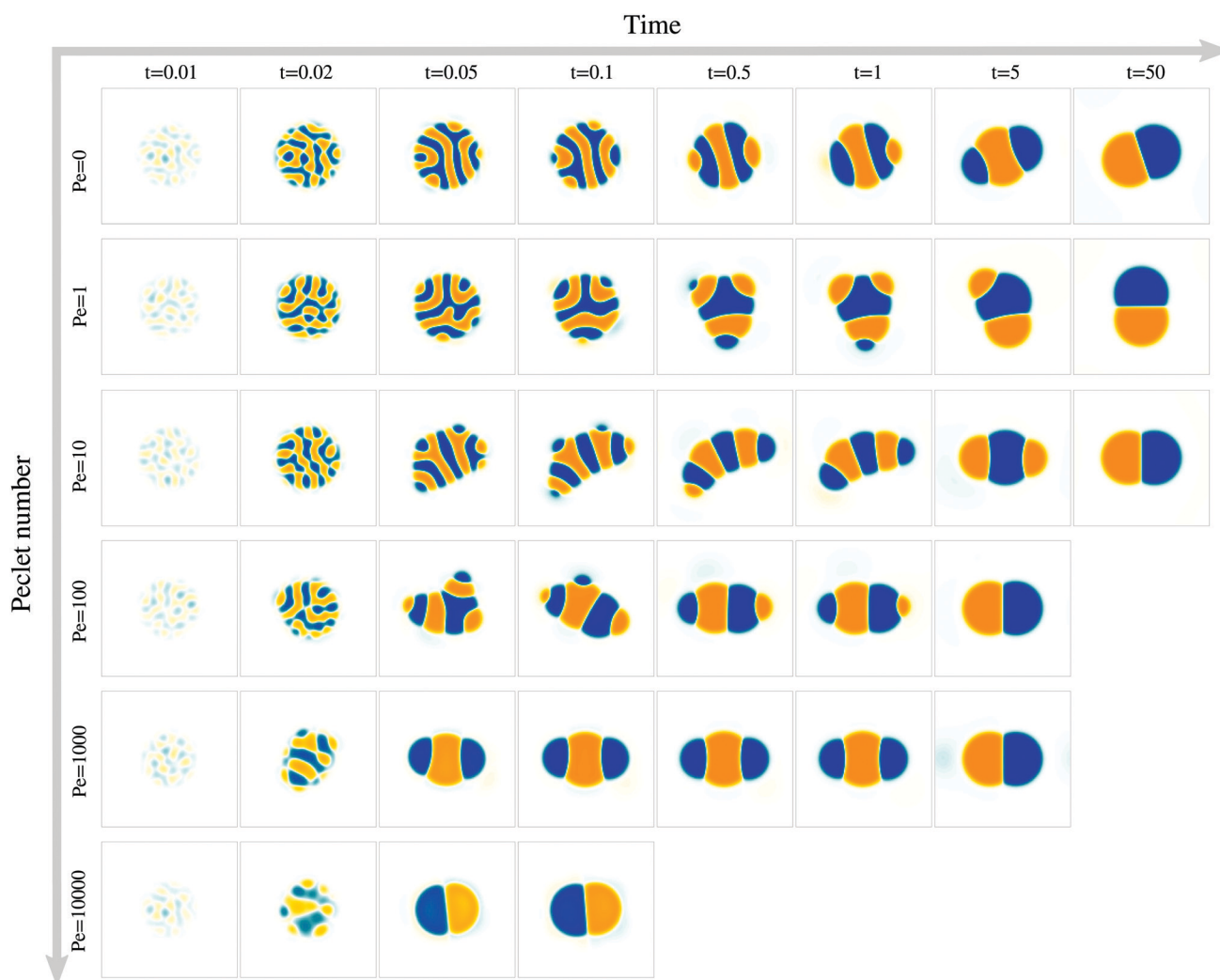

Fig. 2 Advection affects the coarsening dynamics and the time to reach the polarized equilibrium state. For each value of the Peclet number, a time series of snapshots is shown, representing the ϕ field from −1 (orange) to 1 (blue). Here we set $\Delta\sigma = 0$, *i.e.* the outer surface tension is independent of ϕ.

Leading up to this equilibrium state, we find well-known features of spinodal decomposition, including an initial decomposition phase where $|\phi|$ generally grows until it saturates at ≈ 1, and a subsequent coarsening phase. However, Fig. 2 also suggests (1) that increasing the Peclet number speeds up the phase separation process (discussed below in this section),[1] and (2) that intermediate Peclet numbers give rise to long-lived strongly elongated droplets (discussed in the next Section 3.2).

To quantify in how far increasing the Peclet number speeds up the droplet polarization process, we measure the time evolution of a dipole moment, which we define as

$$\boldsymbol{P}(t) = \int_{\Omega} \phi(1-\psi)(\boldsymbol{x}-\boldsymbol{c})\mathrm{d}A. \quad (10)$$

Here, $\boldsymbol{c}$ is the barycenter of the droplet, defined as $\boldsymbol{c} = \int_{\Omega}(1-\psi)\boldsymbol{x}\mathrm{d}A / \int_{\Omega}(1-\psi)\mathrm{d}A$. We study the normalized magnitude $p = |\boldsymbol{P}|/P_0$, where $P_0 = L^3/6$ is a reference dipole moment, which corresponds to a circular droplet of diameter L split in two semi-circular regions with $\phi = 1$ and $\phi = -1$. We find that indeed, the dipole moment p grows faster for higher Peclet number (Fig. 3a). We moreover define a polarization time t_{p} of the system as the time when the polarization first reaches $p \geq 0.9 p_{\mathrm{eq}}$, where p_{eq} is the dipole moment of the equilibrium state. Consistent with known results from the literature,[1] we find that advection speeds up the phase separation process (Fig. 3b). However, we note this effect only for Pe $\gtrsim 100$, while t_{p} remains approximately constant for Peclet numbers below 100. To better understand this Pe dependence of the polarization process, we now discuss the different phases of the process separately.

Initial decomposition. We quantify the phase field amplitude $|\phi|$ during the initial decomposition phase, which lasts until the time $t_{\mathrm{d}} \approx 0.02\tau_{\mathrm{D}}$. To this end, we use the spatial root mean square $\hat{\phi}$ (RMS) of ϕ, defined as $\hat{\phi}^2 = \int_{\Omega}(1-\psi)\phi^2\mathrm{d}A / \int_{\Omega}(1-\psi)\mathrm{d}A$. Fig. 3c shows that $\hat{\phi}$ initially increases exponentially, and reaches a saturation at approximately t_{d}. Except for very large Pe, the behavior during this initial phase does not depend very strongly on the Peclet number.

Coarsening. We find that the subsequent coarsening phase is strongly affected by the Peclet number. This is apparent in Fig. 3d, where we plot the time evolution of the typical domain size λ (exact definition in ESI†). For Pe = 0, the domain size λ coarsens according to a power law with an approximately constant exponent close to 1/3. In 2D, this is indeed the predicted exponent for systems that coarsen exclusively through the motion and deformation of domain boundaries.[1]

For very large Peclet number, Pe $\gtrsim 10^3$, we observe a coarsening exponent close to one (Fig. 3d), which corresponds to the expected result for advection-dominated coarsening. For such large Pe numbers, advection even induces noticeable coarsening already during the initial decomposition phase (Fig. 3d). This early coarsening is also the likely reason for the slowing down of the initial decomposition for very large Pe
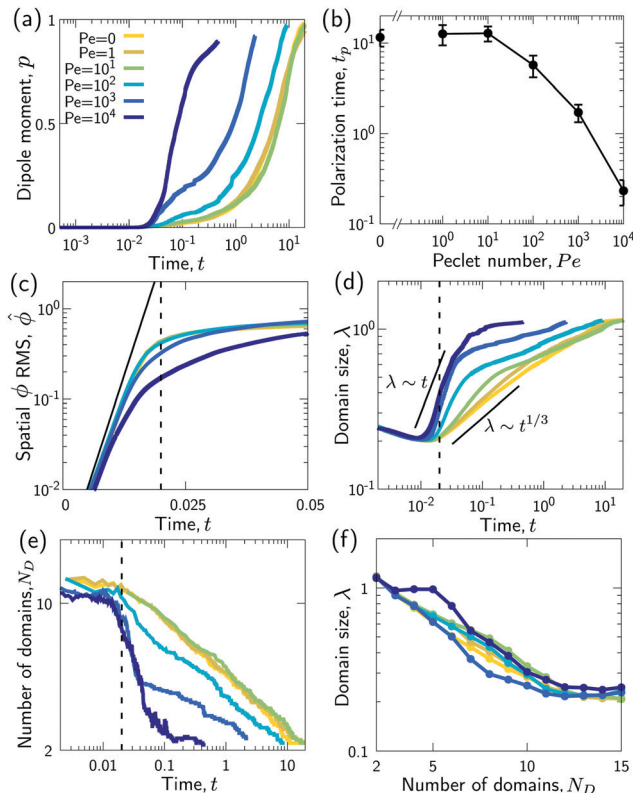

Fig. 3 Advection speeds up droplet polarization by accelerating the coarsening phase. (a) Dipole moment p depending on time for different Pe. (b) Polarization time t_{p} as a function of the Peclet number; error bars indicate the standard error of the mean. (c) Spatial root-mean-square of ϕ depending on time. The black line shows the initial growth with rate ω predicted by linear stability analysis, $\hat{\phi} \sim \mathrm{e}^{\omega t}$. (d) Domain size λ as defined in the ESI,† depending on time. (e) Number of phase domains N_{D} depending on time. (f) Domain size λ as a function of the number of phase domains N_{D}. Legends in panels c–f same as in panel a. In panels c–e, the vertical dashed line indicates the approximate end time $t_{\mathrm{d}} \approx 0.02\tau_{\mathrm{D}}$ of the initial decomposition phase. The quantities on all ordinate axes are averaged over 25 simulation runs.

(Fig. 3c), since diffusive unmixing needs to act over larger length scales in this regime.

The difference in the coarsening behavior between small and large Peclet number is also apparent when studying the behavior of the number of phase domains N_{D} (Fig. 3e). We computationally define a phase domain as a connected region with constant sign of ϕ. The number of domains N_{D} decreases during the coarsening process until it reaches a minimum of two, which is attained in the equilibrium state. Indeed, N_{D} decreases more rapidly for larger Peclet number (Fig. 3e). This confirms that advection speeds up the coarsening process, as N_{D} and λ are strongly correlated (Fig. 3f).

For intermediate Peclet number, we initially observe a relatively fast coarsening (Fig. 3d). However, coarsening subsequently significantly slows down, which is also the reason why the polarization time t_{p} decreases only for very large Pe (compare Fig. 3b and d). What could be responsible for this slow down?

3.2 Elongated, striped droplets at intermediate Pe

We wondered whether the elongated, striped droplets that emerge for intermediate Pe (Fig. 2) could be related to the slow down of the coarsening at intermediate Pe numbers. To test this hypothesis, we quantified the time evolution of droplet elongation E. We define E by expressing the droplet shape in polar coordinates and computing the second angular Fourier mode (Fig. 4a, details in ESI†). It is normalized such that E corresponds to the maximal radius variation of the second Fourier mode relative to the initial droplet radius $r_0 = L/2$.

We find that for Pe = 0, where the droplet changes its shape through diffusive processes only, and very large Pe, where advection dominates, the droplet elongation E monotonically

increases with time until $E \approx 0.2$ (Fig. 4b), which corresponds to the elongation of the final equilibrium state. However, for intermediate Pe, droplet elongation first increases as high as $E \approx 0.3$ before decreasing back to the final value of ≈ 0.2. Moreover, this regime of transient elongation is correlated in time to the phase of slow coarsening (compare Fig. 3d and 4b). This suggests that the elongated droplet structures could indeed be related to the observed coarsening slow down for intermediate Pe.

Because the temporal coarsening dynamics differs when varying the Pe number, we also plot the droplet elongation over the number of domains N_D. This allows to compare droplet elongation E at similar "stages" of the coarsening process
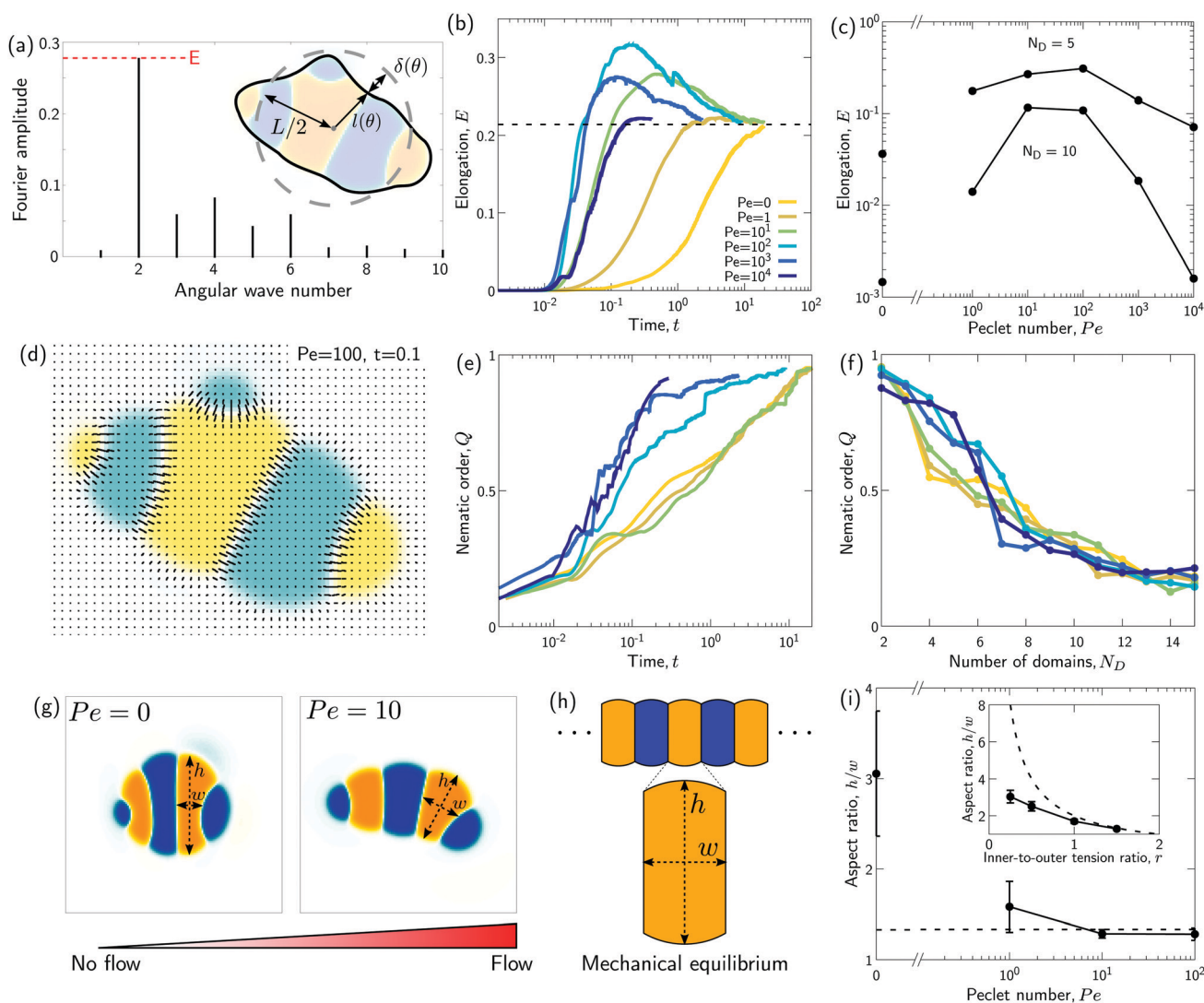

Fig. 4 Transient "croissant" states, which are elongated and show a striped organization of the phase domains. (a) Illustrative example of droplet surface deformation, at Pe = 100 and t = 0.1, and resulting angular Fourier spectrum used to define the droplet elongation E. (b) Evolution of the droplet elongation as a function of time. (c) Transient droplet elongation as a function of the Peclet number at fixed numbers of phase domains, N_D. (d) Illustrative nematic field based on the ϕ-field gradient, at Pe = 100 and t = 0.1. (e and f) Evolution of the global nematic order as a function of (e) time and (f) N_D, for different Peclet numbers. (g) Comparison for two snapshots for Pe = 0 and Pe = 10 with N_D = 5. (h) Limiting case of infinite chain of equally-sized phase domains in mechanical equilibrium, where $h/w = 2/r$ (see ESI†). (i) Phase domain aspect ratio h/w as of function of Pe for r = 1.5. (i inset) Aspect ratio over inner-to-outer tension ratio r for Pe = 10. The aspect ratio is averaged over all domains having exactly two neighboring domains (i.e. all non-branching inner domains) for time points with N_D = 5. The quantities in all panels are averaged over a series of 25 simulations.

across different Pe numbers. We find that at the same N_D, elongation can be up to two orders of magnitude larger for intermediate Pe (Fig. 4c).

We also observe in Fig. 2 that elongated droplets show striped domain patterns. Such a striped arrangement could indeed help to explain the observed coarsening slow down even for intermediate Pe. A striped pattern of domains could be close to a mechanical equilibrium where only little hydrodynamic flows occur. In this case, coarsening would occur almost entirely through diffusion in an Ostwald-ripening-like process: Due to an increased Laplace pressure in small stripes as compared to larger stripes of the same color, the larger domain would slowly grow at the expense of the smaller domain through diffusive fluxes across the domains of opposite color.

To test these ideas and to better understand how elongated droplet shapes emerge, we quantify the nematic order of inner domain boundaries (*i.e.* between droplet domains 1 and 2) by an order parameter Q (Fig. 4d). To this end, we first introduce a tensor field $A_{\alpha\beta}$ that characterizes the local orientation of ϕ interfaces (Fig. 4d):

$$A_{\alpha\beta} = (1 - \psi)\frac{\partial\tilde{\phi}}{\partial x_\alpha}\frac{\partial\tilde{\phi}}{\partial x_\beta}. \tag{11}$$

Here, Greek letters are dimension indices and we use the normalized field $\tilde{\phi} = (C_1 - C_2)/(C_1 + C_2) = \phi/(1 - \psi)$. We then introduce the tensor $Q_{\alpha\beta}$ as the spatially averaged, symmetric, traceless part of $A_{\alpha\beta}$:

$$Q_{\alpha\beta} = \frac{1}{\langle A_{\gamma\gamma}\rangle}\left\langle A_{\alpha\beta} - \frac{1}{2}\delta_{\alpha\beta}A_{\gamma\gamma}\right\rangle. \tag{12}$$

Here, Einstein notation is used and the brackets $\langle\cdot\rangle$ denote spatial averaging over the system. We define the magnitude of the nematic order parameter as $Q = \sqrt{Q_{xx}^2 + Q_{xy}^2}$. When the domain interfaces are randomly oriented, nematic order vanishes, $Q = 0$, while when all domain interfaces are straight and perfectly aligned, $Q = 1$.

Generally, the nematic interface alignment Q increases over time, and it does so more quickly for large Pe numbers (Fig. 4e). Note that the final equilibrium state has $Q \approx 1$, because it consists of a single straight internal interface. Notably, if we plot Q over N_D, we find no strong difference across Pe numbers (Fig. 4f). Indeed, Fig. 2 also show striped domain patterns not only for intermediate Pe, but also for Pe = 0. But if the domain pattern is also striped for Pe = 0, then why do we find elongated droplets only for intermediate Pe (Fig. 4g)?

A possible reason for why Pe > 0 droplets are more elongated is that hydrodynamic flows would drive the system closer to mechanical equilibrium, where in mechanical equilibrium the droplets might be elongated. To test these ideas, we first analytically compute the mechanical equilibrium state for a striped droplet. For simplicity, we focus on the limiting case of an infinite chain of equally sized domains (Fig. 4h). In mechanical equilibrium with $\Delta\sigma = 0$, interfaces between phases 1 and 2 are parallel straight lines, and surfaces to the external fluid 3 are circular arcs. One can furthermore show that the aspect ratio of a single domain in mechanical equilibrium depends only on the inner-to-outer tension ratio r as $h/w = 2/r$ (derivation in ESI†). Thus, in a crude approximation, a droplet with N_D domains in mechanical equilibrium would have aspect ratio $N_D w/h = N_D r/2$.

To test whether droplets for intermediate Pe approach the mechanical equilibrium state, we quantified the domain aspect ratio h/w in our simulations (details in ESI†). We plot h/w for $r = 1.5$ depending on Pe in Fig. 4i and compare to the theoretical solution of the infinite chain (dashed line). Our results suggest that the droplets do indeed approach mechanical equilibrium as Pe increases.

To further test these ideas, we compared domain aspect ratios also across different values of the inner-to-outer tension ratio r (Fig. 4i inset). We found that for smaller r, the measured aspect ratio started to become smaller than the theoretical prediction. This makes sense since for smaller r, the overall droplet aspect ratio also becomes smaller and so the simulated droplets deviate more strongly from the theoretical picture of a chain of equally sized domains. Indeed, for $r \to 0$, the infinite-chain prediction would be $h/w = 2/r \to \infty$. However, in this limit, there is no inner interface tension, $\sigma_{12} = 0$, and the droplet shape is spherical. When dividing a spherical droplet into N_D domains of equal width, the domain aspect ratio is $h/w \leq N_D$, which corresponds to an approximate upper bound for h/w.

Taken together, our results show that for intermediate Pe, transient droplet states form, which are striped and elongated. They are close to mechanical equilibrium and coarsen only through diffusive fluxes, which makes them long-lived.

3.3 Effect of a difference between the surface tensions of the two droplet phases

We next study the effect of different surface tensions between the two droplet phases, $\Delta\sigma \neq 0$. To this end, we carried out simulations with varying $0 \leq \Delta\sigma < 1$ for the Peclet numbers 0, 100, and 10^4 (Fig. 5, Movies S1–S9, ESI†).

We first examined how varying the surface tension difference $\Delta\sigma$ would change the time t_p required to reach the polarized equilibrium state (Fig. 6a). Although a Janus droplet is the equilibrium state for the chosen parameter regime, the system can exhibit very long-lived rotationally symmetric patterns. This is particularly true for Pe = 0, where only simulations with $\Delta\sigma = 0$ and $\Delta\sigma = 0.4$ reached the polar equilibrium state within the maximal simulation time of $t_{max} = 50$. For the two larger Pe values, the equilibrium state was always reached after a finite time t_p, but no clear trend in the dependency on $\Delta\sigma$ is apparent. To better understand these results, we again separately discuss several phases of the process.

Initial decomposition. For $\Delta\sigma > 0$, the initial decomposition into the two droplet phases proceeds from the droplet boundary inwards in concentric circles (Fig. 6b). This phenomenon is called composition wave in the literature:[35,36] For $\Delta\sigma > 0$, fluid 2 (orange) has a lower surface tension, and so a stripe with an abundance of fluid 2 first appears close to the surface. This supplants fluid 1 (blue) in this region, pushing it further
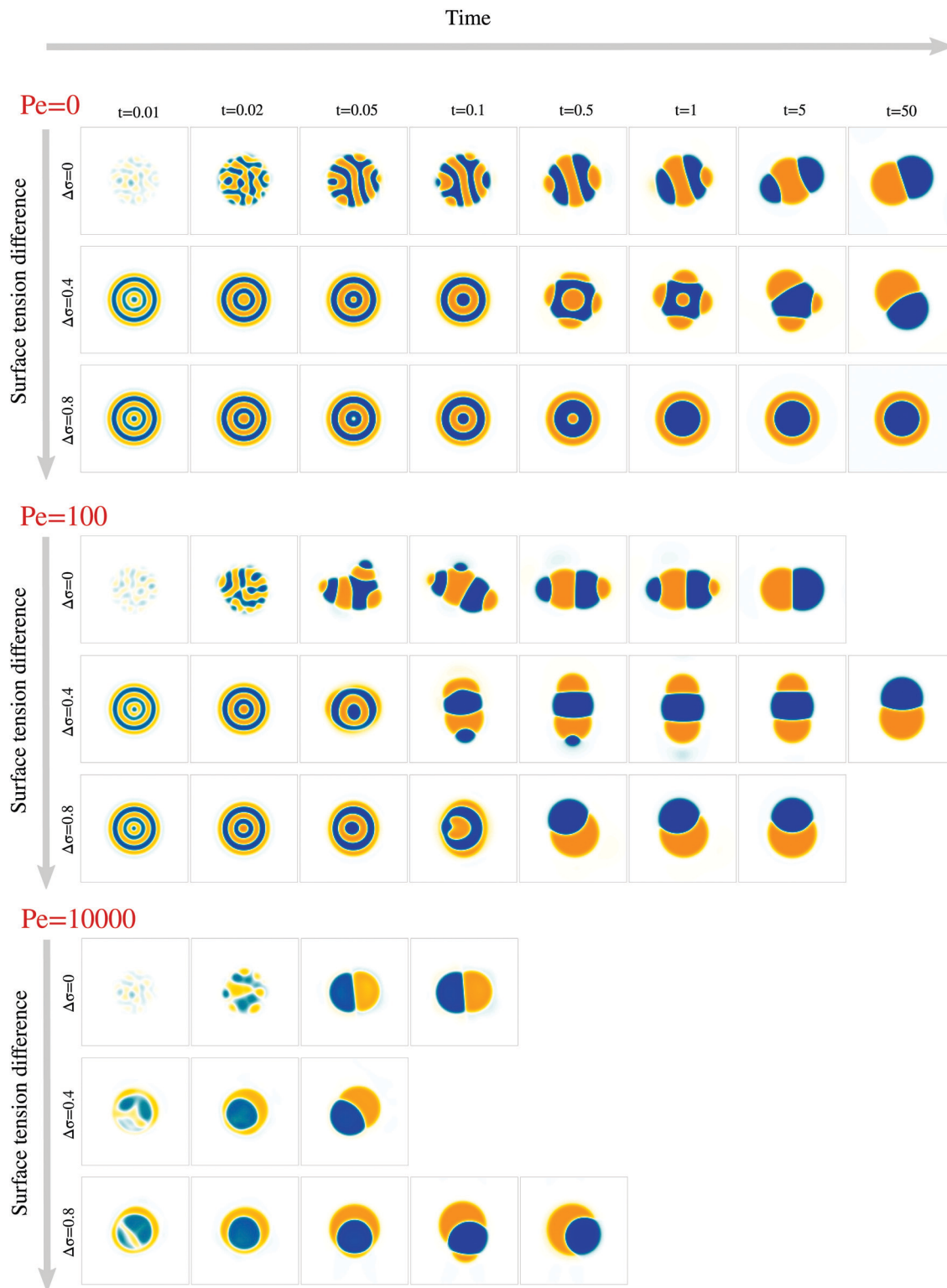
Fig. 5 Surface tension difference affects transient droplet morphologies and polarization time. For different values of $\Delta\sigma$ and Pe, a time series of snapshots is shown, representing the ϕ field from -1 (orange) to 1 (blue).

inwards. The slight abundance of fluid 1 next to the outer fluid-2 stripe attracts more of fluid 1, supplanting more of fluid 2, some of which is pushed further inwards, and so on. This initial decomposition proceeds until the whole droplet displays a rotationally symmetric striped pattern, where the stripes reach saturation $|\phi| \approx 1$ again around $t_{\mathrm{d}} \approx 0.02\tau_{\mathrm{D}}$.

Coarsening. The rotationally symmetric pattern coarsens through progressive broadening of the stripes and occasional
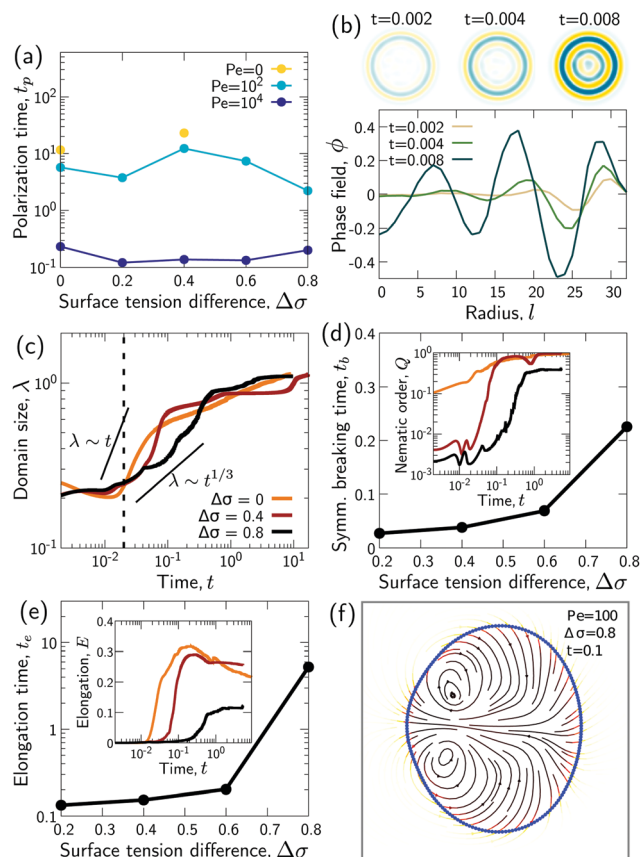
Fig. 6 (a) Polarization time as a function of $\Delta\sigma$. (b) Composition wave during the initial decomposition phase, for Pe = 100 and $\Delta\sigma$ = 0.4. (c) Domain size λ as a function of time. (d) Symmetry breaking time t_b over $\Delta\sigma$. The symmetry breaking time t_b is the first time when the nematic order Q of inner domain boundaries increases above a value of 0.01. (d inset) Nematic order Q of the inner domain boundaries over time for different $\Delta\sigma$. Legend same as in panel c. (e) Time t_e when a croissant state (or a Janus droplet) emerges over $\Delta\sigma$. The time t_e is defined as the first time when droplet elongation E reaches 90% of its maximum value. (e inset) Droplet elongation E over time for different $\Delta\sigma$. Legend same as in panel c. (f) Directional flow during symmetry breaking. In panels b–f: Pe = 100. In each of the panels c–e incl. insets, the respective quantity on the ordinate axis is averaged over 25 simulation runs.

annihilation of the innermost phase domain (Fig. 5 and 6c). For most simulations with Pe = 0, the system most often remained in a state with two concentric phase domains during the whole simulation time (*e.g.* Fig. 5, for Pe = 0, $\Delta\sigma$ = 0.8). However, for finite Peclet number, this rotational symmetry got broken; for Pe = 100 during the coarsening phase, and for Pe = 10^4 already during the initial decomposition phase.

Symmetry breaking. While there is no clear correlation of the polarization time t_p with $\Delta\sigma$, we wondered whether at least the time of symmetry breaking shows a clear dependence on $\Delta\sigma$. We thus defined the time of symmetry breaking t_b as the first time when the nematic order of the inner domain boundaries, Q, surpassed a value of 0.01. For Pe = 100, we found indeed that t_b increased monotonically with $\Delta\sigma$ (Fig. 6d & inset).

Transient flows. The symmetry breaking usually triggered complex transient hydrodynamic flows that were qualitatively similar in different parts of the parameter space, and reminiscent of Marangoni flows within a droplet (Fig. 6f).[37,38] For Pe = 100, these flows typically resulted in a croissant state.

Slowly relaxing croissant state. We wondered whether also the time t_e it takes for the croissant state to emerge shows a clear dependence on $\Delta\sigma$. We defined t_e as the first time when the droplet elongation E reached 90% of its maximum value during any given simulation. This captures both the approximate time of maximum elongation, in cases where a croissant state was created, or the time when E first reached the final plateau value, in cases where the transient flows directly created a 2-phase Janus droplet. We find that t_e does indeed increase monotonically with $\Delta\sigma$ (Fig. 6e & inset).

Thus, while the time t_p for the whole process varies non-monotonically with $\Delta\sigma$, the time t_e when the croissant state appears increases monotonically but is generally much smaller than t_p (compare Fig. 6a and e). This means that the variation in t_p is due to a variation in the life time of the croissant states. In the previous section, we concluded that for intermediate Pe, these states coarsen only due to an Ostwald-ripening-like process, where smaller domains shrink at the expense of larger ones. This suggests that the variation in t_p may just be due to the way the two droplet phases happen to be distributed into different domains by the transient flows that follow the symmetry breaking. Indeed, we find for instance that for Pe = 100, the simulations with $\Delta\sigma$ = 0.4 need longest to relax to the 2-domain equilibrium state (Fig. 6a), and these are also the simulations where two approximately equally-sized orange domains form (Fig. 5), leading to an initially slow diffusion between the two domains.

Finally, in simulations with Pe = 10^4, a first symmetry breaking event occurred at a time around 0.01. The ensuing transient flows often resulted in a second approximately rotationally symmetric state with 2 domains at a time around 0.02. This state only later resolved into the polar equilibrium state. We believe this second, 2-domain rotationally symmetric state forms in this case because the first breaking of rotational symmetry occurs before the initial decomposition is finished, *i.e.* when $|\phi|$ is significantly smaller than one within the domains. As a consequence, the interface tension between both domains, which scales as $\sim\phi^2$, is smaller, and thus the *effective* value of $\Delta\sigma = (\sigma_{13} - \sigma_{23})/\sigma_{12}$ is larger than its *nominal* value. Hence, we believe that we find the rotationally symmetric 2-domain state as transient state, because the expected equilibrium state is the rotationally symmetric one as long as the *effective* $\Delta\sigma$ is larger than one (Fig. 1f).

4 Discussion

In this article, we discussed phase separation in a two-phase deformable droplet. While the thermodynamic equilibrium state for such a system is well known, we studied the route to reach equilibrium. In particular, we focused on the interplay

between spinodal decomposition and advection with hydrodynamic flows created by interface tensions. While this interplay has been studied before,[4] it was unknown how it plays out in a finite, deformable system. We found that advection can speed up the coarsening process as reported earlier.[1]

We moreover found that for intermediate Pe numbers, elongated, striped droplet states emerge, which we call "croissant" states. The stripes correspond to a nematic alignment of inner domain boundaries, which emerges for low and intermediate Pe. For intermediate Pe, the striped droplets elongate as they approach mechanical equilibrium. These states are long-lived, because they coarsen almost exclusively via diffusion, through an Ostwald-ripening-like process. We did not observe such "croissant" states for very large Pe numbers, where coarsening is entirely dominated by advection, which leads to coalescence of the phase domains before a striped pattern can develop (Movie S3, ESI†).

We also studied the effect of an asymmetry between the surface tensions of the two droplet phases, and we found that it changes in particular the beginning of the phase separation process. The emergence of composition waves initially creates a rotationally symmetric system, which then starts to coarsen diffusively. Breaking of this rotationally symmetric state triggers transient flows that are reminiscent of Marangoni flows in droplets.[37,38] These transient flows typically gave rise to a long-lived croissant state. Taken together, our results demonstrate that advection can play an important role in the coarsening dynamics of deformable two-phase droplets.

The croissant states that we observe are reminiscent of past observations made in the field. First, similar observations have been made in ternary phase separation starting from homogeneous states, even for Pe = 0.[28,39] However, with a circular droplet as initial state (Fig. 1c), the emergence of an elongated croissant requires large deformations, which are promoted by advective effects. Second, striped and elongated states can also be observed in vesicles on whose surface different phases coexist.[40,41] However, while the croissant states in our study are created by the interface tensions between bulk phases, the vesicle shapes are affected by the constant surface area, line tensions between phases on the surface, and a phase-dependent free energy of the membrane curvature. Thus, the pattern- and shape-forming mechanisms in these two kinds of systems are likely quite different.

It would be interesting to test whether the croissant states can be reproduced experimentally. Indeed, e.g. multi-component emulsion droplets are receiving continuing attention[42–44] given their applications in the food and pharmaceutical industries.[45] The croissant states might open up new avenues in these areas.

5 Symmetry breaking in stem cell aggregates

This work has also important implications for the kinds of biological systems that originally motivated this study.[22,23,26,27,46–48] Aggregates of stem cells that mimic early vertebrate axis formation are known to develop a polar structure (Fig. 1a and b),[22] reminiscent of two-phase Janus droplets in thermodynamic equilibrium (Fig. 1d), where the different phases correspond to different cell types. While current studies of such stem cell colonies focus almost exclusively on the biochemical dynamics,[49,50] tissue flow and advection likely play an important role as well. Indeed, recent experiments have identified significant large-scale tissue flows in stem cell aggregates.[26]

As a first rough estimate, the Peclet number in mouse embryonic stem cell aggregates is of the order of $Pe \sim L\sigma/D\eta \sim 200$. This is based on an aggregate size of $L \sim 200$ μm,[26] a tension-to-viscosity ratio of $\sigma/\eta \sim 5$ μm h^{-1},[51] and a diffusion constant of order $D \sim 5$ μm^2 h^{-1} (unpublished preliminary data, lab of Pierre-François Lenne). In this Pe regime, we observe in our simulations the emergence of the croissant states. Indeed, these states appear visually reminiscent of somites, which have also been observed to form in gastruloids,[27] while an interface tension has been reported at somite–somite boundaries in vivo.[52] However, first, the mechanism of somite formation in vertebrates is generally believed to crucially involve the complex interplay of biochemical signals in a clock-and-wavefront model[53] (even though purely mechanical models are discussed as well[54]). Second, different from our model, gastruloids exhibit a polar organization before somites form.[27] This raises the question why in experiments there are usually no croissant states observed before polarization.

Stem cell cultures are of course much more complex than the model we studied here, and future refined studies should take additional effects into account. First, experiments indicate that the dynamics of some biological signaling molecules and transcription factors is non-conserving in these systems.[26,49,50] To take this into account in our model, a source term needs to be added in the ϕ equation eqn (6a). Similarly, we studied here a droplet of constant volume, while the stem cell colonies are typically growing. To implement this, source terms need to be added to the ψ dynamics eqn (6b) and in the incompressibility condition eqn (7a).

Second, we focused here on a 2D model, while the stem cell systems motivating this study are 3D aggregates.[22,26] While there are likely several commonalities between the 2D and 3D cases, we expect differences for instance due to Laplace pressure effects.[36,55,56] Such effects arise only in 3D, where in tube-shaped phase domains, interface tension creates a Laplace pressure that depends on the tube radius. This pressure can lead to necking and breakup of connected domains in a Plateau-Rayleigh instability,[55] but it can also lead to a pumping effect that makes the surface layer of the droplet grow more rapidly.[36] It will be interesting to dissect the consequences of these effects for a deformable 3D droplet in future work.

Third, while we focused here on the case of a purely liquid aggregate, the rheology is very likely more complicated.[16] Indeed, relatively young mouse stem cell aggregates have been described as visco-elastic solids before,[51] and the buildup of elastic stresses would likely affect the aggregate behavior.

Fourth, the cell aggregates are active systems, and so activity may need to be included for an effective description of symmetry breaking in the aggregates.[57,58]

Fifth, additional hydrodynamic fields may be required to fully account for some features of the stem cell aggregate dynamics. In particular, the inclusion of more scalar fields in addition to ϕ may be required,[49,50] or of a polar field as experiments on fish aggregates have pointed to a role of polarity proteins.[59,60]

Finally, the real system dynamics is likely influenced by several types of noise. Moreover, a ϕ-dependence of mechanical properties such as viscosity or local volume growth may be required to explain some of the experimental observations.[61]

Conflicts of interest

The authors declare no conflict of interest.

Acknowledgements

References

1 A. J. Bray, *Adv. Phys.*, 2002, **51**, 481–587.
2 S. Mao, D. Kuldinow, M. P. Haataja and A. Košmrlj, *Soft Matter*, 2019, **15**, 1297–1311.
3 S. Mao, M. S. Chakraverti-Wuerthwein, H. Gaudio and A. Košmrlj, *Phys. Rev. Lett.*, 2020, **125**, 218003.
4 H. Tanaka and T. Araki, *Phys. Rev. Lett.*, 1998, **81**, 389–392.
5 A. A. Hyman, C. A. Weber and F. Jülicher, *Annu. Rev. Cell Dev. Biol.*, 2014, **30**, 39–58.
6 Q.-X. Liu, A. Doelman, V. Rottschäfer, M. de Jager, P. M. Herman, M. Rietkerk and J. van de Koppel, *Proc. Natl. Acad. Sci. U. S. A.*, 2013, **110**, 11905–11910.
7 C. P. Brangwynne, *J. Cell Biol.*, 2013, **203**, 875–881.
8 R. J. Wheeler and A. A. Hyman, *Philos. Trans. R. Soc., B*, 2018, **373**, 20170193.
9 H.-S. Kuan, W. Pönisch, F. Jülicher and V. Zaburdaev, *Phys. Rev. Lett.*, 2021, **126**, 18102.
10 M. S. Steinberg, *Science*, 1963, **141**, 401–408.
11 R. A. Foty and M. S. Steinberg, *Dev. Biol.*, 2005, **278**, 255–263.
12 E. Cachat, W. Liu, K. C. Martin, X. Yuan, H. Yin, P. Hohenstein and J. A. Davies, *Sci. Rep.*, 2016, **6**, 1–8.
13 J. D. Amack and M. L. Manning, *Science*, 2012, **338**, 212–215.
14 P. L. Townes and J. Holtfreter, *J. Exp. Zool.*, 1955, **128**, 53–120.
15 E.-M. Schötz, R. D. Burdine, F. Jülicher, M. S. Steinberg, C.-P. Heisenberg and R. A. Foty, *HFSP J.*, 2008, **2**, 42–56.
16 P. Marmottant, A. Mgharbel, J. Kafer, B. Audren, J.-P. Rieu, J.-C. Vial, B. van der Sanden, A. F. M. Maree, F. Graner and H. Delanoe-Ayari, *Proc. Natl. Acad. Sci. U. S. A.*, 2009, **106**, 17271–17275.
17 R. Etournay, M. Popović, M. Merkel, A. Nandi, C. Blasse, B. Aigouy, H. Brandl, G. Myers, G. Salbreux, F. Jülicher and S. Eaton, *Elife*, 2015, **4**, e07090.
18 H. Morita, S. Grigolon, M. Bock, S. F. Krens, G. Salbreux and C. P. Heisenberg, *Dev. Cell*, 2017, **40**, 354–366.e4.
19 S. J. Streichan, M. Lefebvre, N. Noll, E. F. Wieschaus and B. I. Shraiman, *Elife*, 2018, **7**, e27454.
20 S. Münster, A. Jain, A. Mietke, A. Pavlopoulos, S. W. Grill and P. Tomancak, *Nature*, 2019, **568**, 395–399.
21 S. Grosser, J. Lippoldt, L. Oswald, M. Merkel, D. M. Sussman, F. Renner, P. Gottheil, E. W. Morawetz, T. Fuhs, X. Xie, S. Pawlizak, A. W. Fritsch, B. Wolf, L.-C. Horn, S. Briest, B. Aktas, M. L. Manning and J. A. Käs, *Phys. Rev. X*, 2021, **11**, 011033.
22 S. C. van den Brink, P. Baillie-Johnson, T. Balayo, A.-K. Hadjantonakis, S. Nowotschin, D. A. Turner and A. Martinez Arias, *Development*, 2014, **141**, 4231–4242.
23 L. Beccari, N. Moris, M. Girgin, D. A. Turner, P. Baillie-Johnson, A.-C. Cossy, M. P. Lutolf, D. Duboule and A. M. Arias, *Nature*, 2018, **562**, 272–276.
24 T. Fulton, V. Trivedi, A. Attardi, K. Anlas, C. Dingare, A. M. Arias and B. Steventon, *Curr. Biol.*, 2020, **30**, 2984–2994.e3.
25 F. Cermola, C. D'Aniello, R. Tatè, D. De Cesare, A. Martinez-Arias, G. Minchiotti and E. J. Patriarca, *Stem Cell Reports*, 2021, **16**, 354–369.
26 A. Hashmi, S. Tlili, P. Perrin, A. Martinez-Arias and P. F. Lenne, *bioRxiv*, 2020, DOI: 10.1101/2020.05.21.105551.
27 S. C. van den Brink, A. Alemany, V. van Batenburg, N. Moris, M. Blotenburg, J. Vivié, P. Baillie-Johnson, J. Nichols, K. F. Sonnen, A. Martinez Arias and A. van Oudenaarden, *Nature*, 2020, **582**, 405–409.
28 C. Semprebon, T. Krüger and H. Kusumaatmaja, *Phys. Rev. E*, 2016, **93**, 033305.
29 R. David, O. Luu, E. W. Damm, J. W. H. Wen, M. Nagel and R. Winklbauer, *Development*, 2014, **141**, 3672–3682.
30 A. Tiribocchi, N. Stella, G. Gonnella and A. Lamura, *Phys. Rev. E: Stat., Nonlinear, Soft Matter Phys.*, 2009, **80**, 026701.
31 M. L. Blow, S. P. Thampi and J. M. Yeomans, *Phys. Rev. Lett.*, 2014, **113**, 248303.
32 A. Doostmohammadi, S. P. Thampi and J. M. Yeomans, *Phys. Rev. Lett.*, 2016, **117**, 048102.
33 R. Eymard, T. Gallouët and R. Herbin, *Handb. Numer. Anal.*, 2000, **7**, 713–1018.
34 S. Gsell, U. D'Ortona and J. Favier, *J. Comput. Phys.*, 2021, **429**, 109943.
35 B. P. Lee, J. F. Douglas and S. C. Glotzer, *Phys. Rev. E: Stat., Nonlinear, Soft Matter Phys.*, 1999, **60**, 5812.
36 H. Tanaka, *J. Phys.: Condens. Matter*, 2001, **13**, 4637.
37 M. Schmitt and H. Stark, *Phys. Fluids*, 2016, **28**, 012106.

38 C. C. Maass, C. Krüger, S. Herminghaus and C. Bahr, *Annu. Rev. Condens. Matter Phys.*, 2016, **7**, 171–193.

39 L.-Q. Chen, *Acta Metall. Mater.*, 1994, **42**, 3503–3513.

40 T. Taniguchi, *Phys. Rev. Lett.*, 1996, **76**, 4444.

41 M. Yanagisawa, M. Imai and T. Taniguchi, *Phys. Rev. Lett.*, 2008, **100**, 1–4.

42 A. S. Utada, E. Lorenceau, D. R. Link, P. D. Kaplan, H. A. Stone and D. Weitz, *Science*, 2005, **308**, 537–541.

43 T. Nisisako, *Curr. Opin. Colloid Interface Sci.*, 2016, **25**, 1–12.

44 N. Wang, C. Semprebon, H. Liu, C. Zhang and H. Kusumaatmaja, *J. Fluid Mech.*, 2020, **895**, A22.

45 M. Iqbal, N. Zafar, H. Fessi and A. Elaissari, *Int. J. Pharmaceutics*, 2015, **496**, 173–190.

46 D. A. Turner, M. Girgin, L. Alonso-Crisostomo, V. Trivedi, P. Baillie-Johnson, C. R. Glodowski, P. C. Hayward, J. Collignon, C. Gustavsen and P. Serup, *et al.*, *Development*, 2017, **144**, 3894–3906.

47 N. Moris, K. Anlas, S. C. van den Brink, A. Alemany, J. Schröder, S. Ghimire, T. Balayo, A. van Oudenaarden and A. M. Arias, *Nature*, 2020, **582**, 410–415.

48 K. Anlas, N. Gritti, D. Oriola, K. Arató, F. Nakaki, J. Le Lim, J. Sharpe and V. Trivedi, *bioRxiv*, 2021, DOI: 10.1101/2021.02.24.432766.

49 F. Etoc, J. Metzger, A. Ruzo, C. Kirst, A. Yoney, M. Z. Ozair, A. H. Brivanlou and E. D. Siggia, *Dev. Cell*, 2016, **39**, 302–315.

50 S. Chhabra, L. Liu, R. Goh, X. Kong and A. Warmflash, *PLOS Biol.*, 2019, **17**, e3000498.

51 D. Oriola, M. Marin-Riera, G. Aalderink, K. Anlas, N. Gritti, J. Sharpe and V. Trivedi, 2020, arXiv:2012.01455.

52 E. Shelton, S. Kim, B. Gross, R. Wu, M. Pochitaloff, I. Lim, E. Sletten and O. Campàs, *bioRxiv*, 2021, DOI: 10.1101/2021.03.27.437325.

53 A. C. Oates, L. G. Morelli and S. Ares, *Development*, 2012, **139**, 625–639.

54 P. Adhyapok, A. M. Piatkowska, M. J. Norman, S. G. Clendenon, C. D. Stern, J. A. Glazier and J. M. Belmonte, *iScience*, 2021, **24**, 102317.

55 E. D. Siggia, *Phys. Rev. A: At., Mol., Opt. Phys.*, 1979, **20**, 595–605.

56 M. S. Hutson, G. W. Brodland, J. Yang and D. Viens, *Phys. Rev. Lett.*, 2008, **101**, 148105.

57 A. Tiribocchi, R. Wittkowski, D. Marenduzzo and M. E. Cates, *Phys. Rev. Lett.*, 2015, **115**, 1–5.

58 C. A. Weber, D. Zwicker, F. Jülicher and C. F. Lee, *Rep. Prog. Phys.*, 2019, **82**, 064601.

59 M. L. Williams and L. Solnica-Krezel, *Elife*, 2020, **9**, 1–25.

60 E. Tjhung, D. Marenduzzo and M. E. Cates, *Proc. Natl. Acad. Sci. U. S. A.*, 2012, **109**, 12381–12386.

61 A. Mongera, P. Rowghanian, H. J. Gustafson, E. Shelton, D. A. Kealhofer, E. K. Carn, F. Serwane, A. A. Lucio, J. Giammona and O. Campàs, *Nature*, 2018, **561**, 401–405.